Measurements of the negative refractive index of sub-diffraction waves propagating in an indefinite permittivity medium

Dmitriy Korobkin,[1] Burton Neuner III,[1] Chris Fietz,[1] Nikoletta Jegenyes,[2] Gabriel Ferro,[2] and Gennady Shvets[1*]

[1]*University of Texas at Austin, Department of Physics, Austin, Texas 78712, USA*
[2]*Universite Claude Bernard Lyon 1, Laboratoire des Multimateriaux et Interfaces, 69622 Villeurbanne, France*
**gena@physics.utexas.edu*

Abstract: An indefinite permittivity medium (IPM) has been fabricated and optically characterized in mid-infrared spectral range (10.7 μm–11.3 μm). Phase and amplitude transmission measurements reveal two remarkable properties of IPMs: (i) transmission of sub-diffraction waves (as short as λ/4) can exceed those of diffraction-limited ones, and (ii) sub-diffraction waves can propagate with negative refractive index. We describe a novel double-detector optical technique relying on the interference between sub-diffraction and diffraction-limited waves for accurate measurement of the transmission amplitude and phase of the former.

OCIS codes: (120.3180) Interferometry; (160.3918) Metamaterials; (050.6624) Subwavelength structures; (070.7345) Wave propagation; (120.5050) Phase measurement.

References and links

1. D. R. Smith, and D. Schurig, "Electromagnetic wave propagation in media with indefinite permittivity and permeability tensors," Phys. Rev. Lett. **90**(7), 077405 (2003).
2. Z. Jacob, L. V. Alekseyev, and E. Narimanov, "Optical Hyperlens: Far-field imaging beyond the diffraction limit," Opt. Express **14**(18), 8247–8256 (2006).
3. A. Salandrino, and N. Engheta, "Far-field subdiffraction optical microscopy using metamaterial crystals: Theory and simulations," Phys. Rev. B **74**(7), 075103 (2006).
4. I. V. Lindell, S. A. Tretyakov, K. A. Nikoskinen, and S. Ilvonen, "BW media - media with negative parameters, capable of supporting backward waves," Microw. Opt. Technol. Lett. **31**(2), 129–133 (2001).
5. P. A. Belov, "Backward waves and negative refraction in uniaxial dielectrics with negative dielectric permittivity along the anisotropy axis," Microw. Opt. Technol. Lett. **37**(4), 259–263 (2003).
6. A. J. Hoffman, L. Alekseyev, S. S. Howard, K. J. Franz, D. Wasserman, V. A. Podolskiy, E. E. Narimanov, D. L. Sivco, and C. Gmachl, "Negative refraction in semiconductor metamaterials," Nat. Mater. **6**(12), 946–950 (2007).
7. A. J. Hoffman, A. Sridhar, P. X. Braun, L. Alekseyev, S. S. Howard, K. J. Franz, L. Cheng, F.-S. Choa, D. L. Sivco, V. A. Podolskiy, E. E. Narimanov, and C. Gmachl, "Midinfrared semiconductor optical metamaterials," J. Appl. Phys. **105**(12), 122411 (2009).
8. P. A. Belov, and Y. Hao, "Subwavelength imaging at optical frequencies using a transmission device formed by a periodic layered metal-dielectric structure operating in the canalization regime," Phys. Rev. B **73**(11), 113110 (2006).
9. X. Li, S. He, and Y. Jin, "Subwavelength focusing with a multilayered Fabry-Perot structure at optical frequencies," Phys. Rev. B **75**(4), 045103 (2007).
10. M. A. Noginov, H. Li, Y. A. Barnakov, D. Dryden, G. Nataraj, G. Zhu, C. E. Bonner, M. Mayy, Z. Jacob, and E. E. Narimanov, "Controlling spontaneous emission with metamaterials," Opt. Lett. **35**(11), 1863–1865 (2010).
11. D. R. Smith, P. Kolinko, and D. Schurig, "Negative refraction in indefinite media," J. Opt. Soc. Am. B **21**(5), 1032–1043 (2004).
12. D. R. Smith, D. Schurig, J. J. Mock, P. Kolinko, and P. Rye, "Partial focusing of radiation by a slab of indefinite media," Appl. Phys. Lett. **84**(13), 2244–2246 (2004).
13. D. R. Smith, and D. Schurig, "Spatial filtering using media with indefinite permittivity and permeability tensor," Appl. Phys. Lett. **82**(14), 2215–2217 (2003).
14. T. Taubner, D. Korobkin, Ya. Urzhumov, G. Shvets, and R. Hillenbrand, "Near-field microscopy through a SiC superlens," Science **313**(5793), 1595 (2006).

#133245 - $15.00 USD Received 12 Aug 2010; revised 5 Oct 2010; accepted 5 Oct 2010; published 12 Oct 2010

15. N. Fang, H. Lee, C. Sun, and X. Zhang, "Sub-diffraction-limited optical imaging with a silver superlens," Science **308**(5721), 534–537 (2005).
16. D. O. S. Melville, R. J. Blaikie, and C. R. Wolf, "Submicron imaging with a planar silver lens," Appl. Phys. Lett. **84**(22), 4403–4405 (2004).
17. P. Yao, C. Van Vlack, A. Reza, M. Patterson, M. M. Dignam, and S. Hughes, "Ultrahigh Purcell factors and Lamb shifts in slow-light metamaterial waveguides," Phys. Rev. B **80**(19), 195106 (2009).
18. Z. Jacob, I. Smolyaninov, and E. Narimanov, "Broadband Purcell effect: Radiative decay engineering with metamaterials," arXiv:0910.3981v2 (2009).
19. J. B. Pendry, "Negative refraction makes a perfect lens," Phys. Rev. Lett. **85**(18), 3966–3969 (2000).
20. D. Korobkin, Ya. Urzhumov, and G. Shvets, "Enhanced near-field resolution in mid-infrared using metamaterials," J. Opt. Soc. Am. B **23**(3), 468–478 (2006).
21. S. A. Ramakrishna, J. B. Pendry, M. C. K. Wiltshire, and W. J. Stewart, "Imaging the near filed," J. Mod. Opt. **50**, 1419–1430 (2003).
22. E. A. Ray, M. J. Hampton, and R. Lopez, "Simple demonstration of visible evanescent-wave enhancement with far-field detection," Opt. Lett. **34**(13), 2048–2050 (2009).
23. Y. Xiong, Zh. Liu, C. Sun, and X. Zhang, "Two-dimensional imaging by far-field superlens at visible wavelengths," Nano Lett. **7**(11), 3360–3365 (2007).
24. Z. Liu, H. Lee, Y. Xiong, C. Sun, and X. Zhang, "Far-field optical hyperlens magnifying sub-diffraction-limited objects," Science **315**(5819), 1686 (2007).
25. S. Thongrattanasiri, and V. A. Podolskiy, "Hypergratings: nanophotonics in planar anisotropic metamaterials," Opt. Lett. **34**(7), 890–892 (2009).
26. D. E. Aspnes, "Bounds to average internal fields in two-component composites," Phys. Rev. Lett. **48**(23), 1629–1632 (1982).
27. R. A. Depine, M. E. Inchaussandague, and A. Lakhtakia, "Classification of dispersion equations for homogeneous, dielectric-magnetic, uniaxial materials," J. Opt. Soc. Am. A **23**(4), 949–955 (2006).
28. M. J. Hernandez, G. Ferro, T. Chassagne, J. Dazord, and Y. Monteil, "Study of surface defects on 3C–SiC films grown on Si(111) by CVD," J. Cryst. Growth **253**(1-4), 95–101 (2003).
29. E. D. Palik, ed., *Handbook of Optical Constants of Solids*. (Academic Press, Orlando, Fla., 1985).
30. W. G. Spitzer, D. Kleinman, and D. Walsh, "Infrared properties of hexagonal silicon carbide," Phys. Rev. **113**(1), 127–132 (1959).
31. N. Gedik, and J. Orenstein, "Absolute phase measurement in heterodyne detection of transient gratings," Opt. Lett. **29**(18), 2109–2111 (2004).

1. Introduction

Indefinite permittivity media (IPMs) [1], sometimes called "hyperbolic metamaterials" [2–5], are artificial materials that possess an anisotropic dielectric tensor which is indefinite (it possesses both positive and negative eigenvalues) [1]. For example, uniaxial IPMs with a symmetry axis *z* have the permittivity tensor

$$\overline{\overline{\varepsilon}} = \varepsilon_{\perp}\vec{e}_z\vec{e}_z + \varepsilon_{\parallel}\left(\vec{e}_x\vec{e}_x + \vec{e}_y\vec{e}_y\right),$$

where $\mathrm{Re}(\varepsilon_{\perp})\bullet\mathrm{Re}(\varepsilon_{\parallel}) < 0$. Several approaches to making IPMs have been suggested and experimentally realized, including layered structures consisting of interleaved positive and negative permittivity layers [6–9] and metal-filled porous materials [10]. IPMs exhibit many remarkable and unusual optical properties such as negative refraction [6,7,11], near-field focusing [12], and high-impedance surface reflection [1]. A number of other promising applications, e.g., to spatial filtering [13], have been suggested. But the most exciting applications like super- [14–16] and hyper-lensing [2,3] exploit IPM's unusual property of supporting sub-diffraction (i.e., much shorter than the vacuum wavelength of light) electromagnetic waves.

Unlike conventional positive-permittivity materials capable of transporting only *diffraction-limited* electromagnetic waves with wave numbers $k \le nk_0 = 2\pi n/\lambda_0$ (where λ_0 is vacuum wavelength and *n* is the refractive index), IPMs can support propagating *sub-diffraction* waves defined as electromagnetic waves with wave numbers $k >> k_0 = 2\pi/\lambda_0$. In addition to super- and hyper-lensing, sub-diffraction waves are responsible for a variety of exotic phenomena. It has been recently demonstrated [10] that sub-diffraction waves can dramatically enhance the photonic density of states and increase the spontaneous emission rate of an emitter placed inside or in close proximity of an IPM. Ultrahigh Purcell factors [17]

#133245 - $15.00 USD Received 12 Aug 2010; revised 5 Oct 2010; accepted 5 Oct 2010; published 12 Oct 2010

that can be attributed to IPMs open the route to radiative decay engineering and, potentially, single-photon sources [18]. Another recent counter-intuitive theoretical result [13] is that, in the case of an IPM with $\mathrm{Re}(\varepsilon_\perp) > 0$ and $\mathrm{Re}(\varepsilon_\parallel) < 0$, sub-diffraction waves can propagate through it whereas the diffraction-limited waves are non-propagating/evanescent. This unusual and so far experimentally unproven phenomenon has been referred to [13] as the anti-cutoff.

Probably the most famous example of a layered indefinite permittivity material is the superlens consisting of just a few layers [14–16,19,20] or many layers [8,9,21] which can be used for high-resolution imaging. Conventional imaging uses regular (non-IPM) materials, and small object features are lost because of sub-diffraction wave evanescence. However, IPMs may enhance sub-diffraction waves, thus retaining small image features [19,20,22]. Formally, a lossless superlens corresponds to

$$\varepsilon_\parallel \to 0, \text{ and } 1/\varepsilon_\perp \to 0.$$

Sub-wavelength imaging in IPM structures is not limited only to near field. Such devices as far-field superlens [23], hyperlens [2,3,24], hypergrating [25], and periodic metal-dielectric structures [8,9] have been proposed and experimentally demonstrated. All of them allow sub-wavelength far-field imaging that relies on the property of IPMs to propagate sub-diffraction waves without evanescence.

Despite all the attention devoted to IPMs, there have been no reported experiments aimed specifically at understanding the propagation of the sub-diffraction waves through them. As a result, some of the experimental observations still remain puzzling. For example, in the mid-infrared part of the spectrum (which is the focus of this paper), a record $\lambda/20$ resolution was observed [14] at the superlensing wavelength λ_s corresponding to

$$\mathrm{Re}\left(\varepsilon_\parallel(\lambda_s)\right) = 0, \text{ and } \mathrm{Re}\left(\varepsilon_\perp^{-1}(\lambda_s)\right) \approx 0.$$

Electric field strength (amplitude and phase) on the imaging side of the superlens was recorded at various wavelengths λ using a near-field scanning optical microscope (NSOM). The sharpest amplitude images were recorded at $\lambda = \lambda_s$. In addition to the amplitude profiles of the imaged objects (holes in a metal screen), phase images were also recorded at different wavelengths $\lambda \neq \lambda_s$. It was found that the phase contrast vanished at $\lambda = \lambda_s$ and intensified away from λ_s, with the sign of the phase contrast changing as the wavelength was tuned from the red side of the superlensing wavelength ($\lambda > \lambda_s$) to the blue side ($\lambda < \lambda_s$). While the fundamental physics of this phase contrast effect remains to be fully explained, its practical implications are clear: the combination of phase and amplitude imaging can extend the wavelength range where sub-diffraction imaging by a superlens is possible. The purpose of this paper is to understand the amplitude and phase characteristics of radiation propagating through indefinite permittivity materials, with the special emphasis on sub-diffraction wave propagation. This includes the first experimental demonstration of the anti-cutoff [13] phenomenon and the negative index of the sub-diffraction waves propagating under the anti-cutoff condition.

While diffraction-limited waves can be easily launched into an IPM at any incidence angle [6,7], launching sub-diffraction waves is more challenging. There are two common ways to launch sub-diffraction electromagnetic waves with well-defined values of k inside IPM: using a prism [22] or a diffraction grating [20]. Prisms launch waves with unique values of k, but its magnitude is limited by the prism's index of refraction. Because of the lack of index-matching fluids in mid-IR, the optical interface between the prism and the IPM presents a challenge to this technique. The approach adopted for our experiments is to use a diffraction grating [20] with period d_1, fabricated on the front surface of the IPM. We will refer to this grating as an *object* grating (OG). As illustrated by the inset to Fig. 1(b), a set of Fourier harmonics of order $m = 0, \pm 1, \pm 2\ldots$ can be launched into an IPM using a laser beam with the wavelength λ

#133245 - $15.00 USD Received 12 Aug 2010; revised 5 Oct 2010; accepted 5 Oct 2010; published 12 Oct 2010

incident at an angle θ_i. The wave vectors of these harmonics along the IPM's interface are given by

$$k_{\|}^{m} = \frac{2\pi}{\lambda}\sin(\theta_i) + \frac{2\pi}{d_1}m.$$

When the OG's period $d_1 << \lambda$, sub-diffraction waves correspond to $m = \pm 1, 2\ldots$, while the diffraction-limited waves correspond to $m = 0$. Detecting sub-diffraction waves is yet another challenge. In order to be measured, the large-*k* electromagnetic excitations inside the IPM sample have to be converted to propagating waves. This can be done by the second diffraction grating acting as a *diagnostic* grating (DG) [20,23]. The resulting propagating radiation can be detected and measured in the far field as described below.

In the rest of the paper we describe the results of measuring amplitude and phase characteristics of both sub-diffraction and diffraction-limited waves launched into a multi-layer IPM consisting of materials with positive and negative dielectric permittivities. By conducting experiments over a wide spectral range (10.7 μm < λ < 11.3 μm), we investigate the two possible types of IPMs: Type 1 with $\mathrm{Re}(\varepsilon_{\|}) > 0$ and $\mathrm{Re}(\varepsilon_{\perp}) < 0$ corresponding to $\lambda<\lambda_s\approx$10.97 μm and Type 2 with $\mathrm{Re}(\varepsilon_{\|}) < 0$ and $\mathrm{Re}(\varepsilon_{\perp}) > 0$ corresponding to $\lambda > \lambda_s$. We show experimentally and theoretically that Type 1 IPMs support propagating diffraction-limited and sub-diffraction modes waves, with the former dominant in transmission, and both types of waves have a positive refractive index. On the other hand, the Type 2 IPMs do not support propagating diffraction-limited waves while supporting the propagating *negative-index* sub-diffraction waves. For that reason, sub-diffraction waves become comparable in transmission to diffraction-limited waves. The relative intensity of the sub-diffraction and diffraction-limited waves changes by over an order of magnitude in transmission as the wavelength is swept from the spectral region corresponding to the Type 1 IPMs to that of the Type 2 IPMs. This measurement constitutes the first experimental demonstration of the recently predicted [13] anti-cutoff phenomenon. A novel interferometric technique utilizing two detectors and an optical delay line is used to measure the relative phase advance between the sub-diffraction and diffraction-limited waves as they propagate through the IPM. It is shown that this phase difference changes sign at the superlensing wavelength $\lambda = \lambda_s$. We conjecture that this change of the phase difference at the superlensing wavelength explains the sign change of the phase contrast in the recent superlensing experiments [14].

2. Propagation of radiation through the IPM sample: Theory

The investigated IPM is a symmetric structure consisting of SiO_2 – SiC –SiO_2 layers (205 nm, 410 nm, and 205 nm thick, respectively). The components $\varepsilon_{\|}$ and $\varepsilon_{\perp}$ of the dielectric permittivity tensor of the resulting multi-layer film are

$$\varepsilon_{\|} = \left(\varepsilon_{SiC} + \varepsilon_{SiO_2}\right)/2,\ \varepsilon_{\perp} = 2\varepsilon_{SiC}\varepsilon_{SiO_2}/\left(\varepsilon_{SiC} + \varepsilon_{SiO_2}\right)$$

[26]. Both $\varepsilon_{\|}$ and $\varepsilon_{\perp}$ are strongly frequency-dependent. Figure 1(a) plots the real and imaginary parts of $\varepsilon_{\|}$ and $\varepsilon_{\perp}$. As follows from Fig. 1(a), the transition from Type 1 to Type 2 IPM occurs at the superlensing wavelength $\lambda_s \approx$10.97 μm defined as the wavelength where the real parts of the permittivities of SiC and SiO_2 are equal and opposite:

$$\mathrm{Re}\left(\varepsilon_{SiC}(\lambda_s)\right) = -\mathrm{Re}\left(\varepsilon_{SiO_2}(\lambda_s)\right).$$

The dispersion relation of the waves propagating in the indefinite medium is given by [27],

$$\frac{k_{\|}^2}{\varepsilon_{\perp}} + \frac{k_{\perp}^2}{\varepsilon_{\|}} = \frac{\omega^2}{c^2}, \qquad (1)$$

#133245 - $15.00 USD Received 12 Aug 2010; revised 5 Oct 2010; accepted 5 Oct 2010; published 12 Oct 2010

where the $k_{\|}$ and $k_{\perp}$ are the components of the wave vector parallel and normal to the interface, respectively.

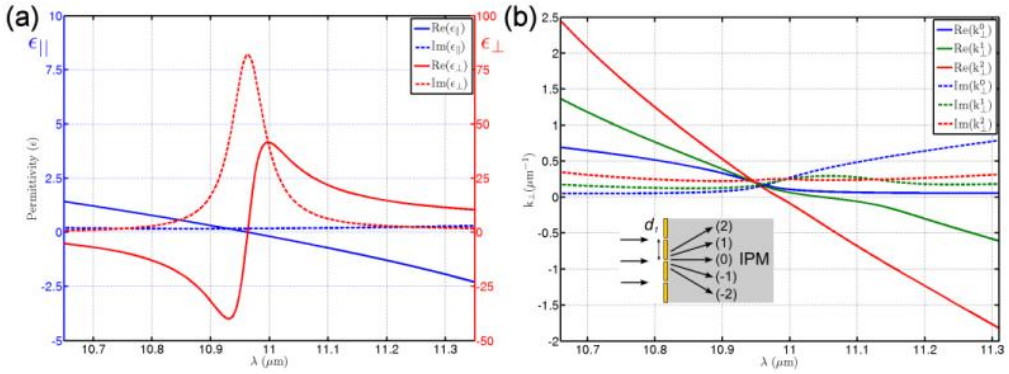

Fig. 1. (a) Parallel and transverse components of the dielectric permittivities of effective anisotropic medium. (b) Real (solid lines) and imaginary (dashed lines) components of $k_{\perp}^{m}$ for m = 0,1,2 Fourier orders. A 0° incident angle is assumed, so $k_{\|}^{m} = 2\pi m / d_1$, and $k_{\perp}^{m}$ are calculated from Eq. (1). The inset shows the excitation of the Fourier orders by the *object* grating.

Sub-diffraction waves are launched into the IPM using a sub-wavelength *object* grating with a period of d_1 = 2.64 μm on the input side of the IPM. Each mode propagates through the IPM with wavenumber $k_{\perp}$ given by Eq. (1). Upon reaching the end of the IPM, each mode is coupled into the vacuum by a *diagnostic* grating with period d_2. The m^{th} mode undergoing the n^{th} order diffractive scattering out of the IPM on the DG acquires a parallel wavenumber given by

$$k_{\|}^{(m,n)} = \frac{2\pi}{\lambda}\sin(\theta_i) + \frac{2\pi}{d_1}m - \frac{2\pi}{d_2}n,$$

where m and n are integers. Equal-period gratings ($d_1 = d_2$) have been used to indirectly infer superlensing [20]. However, in that case all modes scattered into vacuum from the IPM propagate along the same direction coincident with the incidence direction. Therefore, it is impossible to differentiate between the sub-diffractive m = 1 mode and the diffraction-limited m = 0 mode in the far field. However, if the period of the diagnostic grating is slightly different from the object grating ($d_1 \neq d_2$), then each m^{th} sub-diffraction mode scattered by the n^{th} order diffractive scattering on the DG is "released" into the far field into its unique angular direction θ_{mn} given by

$$\sin\theta_{mn} = \sin\theta_i + \lambda\left(\frac{m}{d_1} - \frac{n}{d_2}\right),$$

The condition $|\sin\theta_{mn}| < 1$ must be satisfied for far-field propagation; therefore strongly sub-wavelength OG and DG with similar periods only allow for $m = n$. Thus, a unique scattering angle $\theta_m \equiv \theta_{mm}$ can be assigned to each mode. The presented case of d_1 = 2.64 μm and d_2 = 2.84 μm results in far-field radiation for $m = n$ = 0, 1, 2, and 3. For the rest of the paper we will refer to these modes as the 0th, 1st, 2nd and 3rd order modes respectively, both when they are inside the IPM and after they have been coupled into the far-field by the diagnostic grating.

It is instructive to examine the propagation of these modes inside the Type 1 and Type 2 IPM. Figure 1(b) shows the spectral dependences of the real and imaginary parts of the perpendicular component of wave vector $k_{\perp}$ for the first three modes (one diffraction-limited and two sub-diffraction modes). For the Type 1 IPM, both sub-diffraction and diffraction-

#133245 - $15.00 USD Received 12 Aug 2010; revised 5 Oct 2010; accepted 5 Oct 2010; published 12 Oct 2010

limited waves are propagating, with Re($k_\perp$) > 0. The sign of $k_\perp$ is chosen so that the sign of the imaginary part of $k_\perp$ is positive, indicating that the wave is decaying in the direction away from the interface and into the IPM. More intuitively, the sign of $k_\perp$ can be chosen by examining the expressions for the time-averaged components $S_\perp$ and $S_\parallel$ of the Poynting flux inside the IPM given by:

$$S_\perp = \mathrm{Re}\left[\frac{k_\perp}{\varepsilon_\parallel}\right]\frac{|H_0|^2}{2}, \quad \text{and} \quad S_\parallel = \mathrm{Re}\left[\frac{k_\parallel}{\varepsilon_\perp}\right]\frac{|H_0|^2}{2}, \tag{2}$$

where H_0 is the amplitude of the magnetic field. Because $S_\perp$ must point away from the *object* grating, the sign of $k_\perp$ must coincide with that of $\varepsilon_\parallel$, i.e., positive for the Type 1 IPMs. After a single-pass through the IPM, all propagating modes advance their phases by

$$\varphi_m = \mathrm{Re}\left(k_\perp^m\right) l, \tag{3}$$

where l = 820 nm is the thickness of the sample.

It follows from Eq. (2) that the phase velocity $\vec{v}_{ph} = \vec{k}\omega / k^2$ and group velocity $\vec{v}_{gr} \parallel \vec{S}$ do not coincide with each other. As schematically shown in Fig. 2 (λ=10.7 μm), negative $\varepsilon_\perp$ implies that $S_\parallel$ and $k_\parallel$ have opposite signs causing negative refraction at the interface between the IPM and vacuum because $k_\parallel$ must be continuous across the boundary. This is known as *negative refraction*, and has been experimentally observed [6,7] for diffraction-limited waves in Type 1 IPM. Negative refraction should not be confused with negative refractive index in the propagation direction normal to the interface which, for the Type 1 IPM, is indeed positive as explained above.

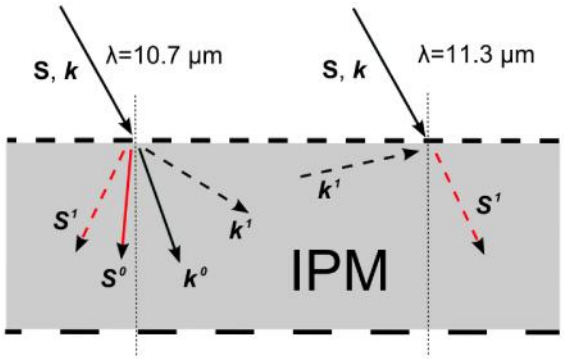

Fig. 2. Directions of Poynting flux (red color) and wave-vector (black color) for 0th (solid line) and 1st (dashed line) Fourier orders at λ=10.7 μm (left) and 11.3 μm using an angle of incidence of 30°. The 0th order is evanescent and not shown for λ=11.3 μm.

The situation changes dramatically for the Type 2 IPM: diffraction-limited waves satisfying 0 < Re($k_\parallel^2/\varepsilon_\perp$) < ω^2/c^2 become evanescent, i.e., $k_\perp^0$ is mostly imaginary. That is the main reason why this type of IPM has not been experimentally explored so far: light incident on the IPM is mostly reflected [6]. On the other hand, sub-diffraction waves satisfying $\mathrm{Re}\left(k_\perp^{i2}/\varepsilon_\perp\right) > \omega^2/c^2 > 0$ are propagating and, according to Fig. 1(b) and Fig. 2 (λ=11.3 μm), possess a *negative refractive index* Re($k_\perp$) < 0 and a relatively small positive imaginary part. For example, at λ=11.3 μm the 1st Fourier order has effective index Re(n_{eff}) = –0.94 and a relatively high figure of merit Re $k_\perp$ /Im $k_\perp$ ~2.8. Even though sub-diffraction waves have a negative refractive index, they do not exhibit negative refraction because $S_\parallel$ and $k_\parallel$ have the same sign.

#133245 - $15.00 USD Received 12 Aug 2010; revised 5 Oct 2010; accepted 5 Oct 2010; published 12 Oct 2010

The directions of Poynting flux and the wave-vectors inside the IPM for 0th and 1st Fourier orders at 10.7 μm (Type 1 IPM) and 11.3 μm (Type 2 IPM) are illustrated by Fig. 2. At 10.7 μm, the refraction angle for the diffraction-limited wave is negative (negative refraction), while its wave-vector has a positive projection on propagation axis (positive index). At 11.3 μm, the diffraction-limited wave is essentially evanescent, so no Poynting vector is drawn. However, the 1st Fourier harmonic can propagate, and the projection of its wave-vector is negative (negative index).

3. Fabrication of the IPM sample

IPM fabrication began with growth of the 410 nm 3C-SiC film on a 400-μm thick Si(100) substrate. Growth was carried out using a two-step atmospheric pressure chemical vapor deposition: substrate carbonization under propane at 1150°C was followed by epitaxial growth using a silane/propane mixture at 1350°C [28]. The growth rate was 3 μm/h. SiC thickness was verified with a Woollam ellipsometer. The silicon side of the SiC/Si wafer was then protected by 6 μm SiO_2 hard mask. A set of 1 mm x 1 mm square openings were fabricated by laser ablation. The entire 400-μm silicon layer was etched in 80°C 35% KOH, forming a set of suspended 410 nm SiC membranes [11]. The anisotropic KOH etch resulted in 350 μm x 350 μm membranes. A 205 nm layer of SiO_2 was deposited (via PECVD) on each surface of the SiC membrane, completing the tri-layer IPM. The dielectric permittivity of SiO_2 was obtained from Ref [29], while that of SiC was calculated from a least-square minimization routine fit to spectral transmission and reflection [20] through the SiC membrane before SiO_2 deposition. The resulting SiC permittivity is given by the standard polaritonic formula [30]

$$\varepsilon_{SiC}(\omega) = \varepsilon_{\infty} \frac{\omega^2 - \omega_{LO}^2 - i\Gamma\omega}{\omega^2 - \omega_{TO}^2 - i\Gamma\omega},$$

where the infinite-frequency permittivity ε_{∞}=6.5, the longitudinal optical phonon mode ω_{LO}=972 cm^{-1}, the transverse optical phonon mode ω_{TO}=796 cm^{-1}, and SiC damping Γ=3.75 cm^{-1}.

The object and diagnostic gratings were fabricated by evaporating 100 nm of Au on both surfaces of the IPM, followed by focused ion beam milling of the two sets of periodic slits in Au films. The periods and slit widths of the fabricated gratings are given as follows: d_1=2.64 μm and w_1=1.1 μm for the OG and d_1=2.84 μm and w_1=0.8 μm for the DG. The milled gratings cover a 300 μm x 300 μm area. Figure 3(a) sketches the IPM structure while 3(b) shows the cross-section with all 5 layers labeled. A Moiré pattern of both gratings in transmitted light (with the Moiré period given by $\Lambda_M = d_1 d_2 / (d_2 - d_1) \approx 37$ μm clearly visible under optical microscopy) and a SEM picture of the *object* grating are shown in 3(c) and 3(d), respectively. Note that the transmission angle of the m^{th} Fourier harmonic of the grating can be recast in terms of the Moiré period in the following form: $\sin\theta_m = \sin\theta_i + m\lambda/\Lambda_M$.

#133245 - $15.00 USD Received 12 Aug 2010; revised 5 Oct 2010; accepted 5 Oct 2010; published 12 Oct 2010

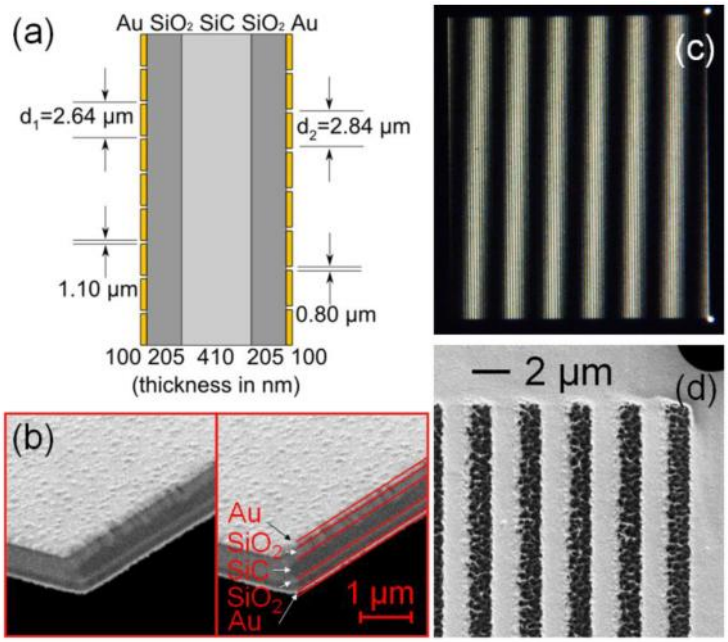

Fig. 3. (a) Schematic of the IPM structure. (b) SEM image of the IPM structure cross-section. (c) Moiré pattern of both gratings in transmitted light. (d) SEM picture of the *object* grating.

4. Intensity measurements: Experimental set-up and results

For complete characterization of radiation propagation through the IPM, both intensity and phase measurements have been performed. We start with the description of intensity measurements. Figure 4 shows the set-up for measuring the intensity of transmitted radiation.

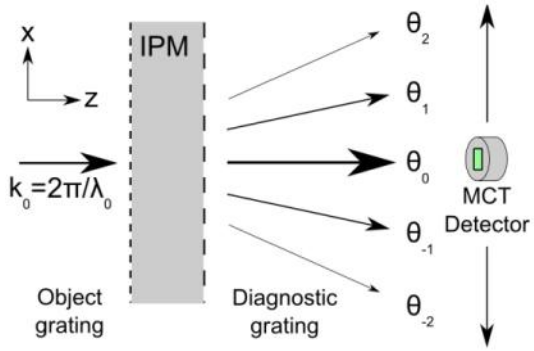

Fig. 4. Experimental set-up for intensity measurements: the incident laser beam scatters at the *object* grating and launches diffraction-limited (0th order) and sub-diffraction (higher order) electromagnetic waves into the IPM. These modes are scattered into the far field towards the detector by the *diagnostic* grating.

Radiation from a line-tunable isotope-filled $^{13}CO_2$ laser was focused by 15 cm focal length ZnSe lens (300 μm spot size) onto the sample. The laser operates in the 10.67 μm–10.85 μm (**R**-branch) and 11.03 μm–11.31 μm (**P**-branch) spectral ranges that conveniently coincide with Type 1 and Type 2 IPMs, respectively. Transmitted radiation was detected by a room temperature MCT detector positioned on a rail perpendicular to the laser beam. This arrangement enabled us to measure the intensities of the different Fourier harmonics of the *object* grating released into the far-field at different angles θ_m. A lock-in amplifier was used to improve the signal-to-noise ratio. Intensities of 0^{th} (diffraction-limited) and $\pm1^{st}$, $\pm2^{nd}$ (sub-

#133245 - $15.00 USD Received 12 Aug 2010; revised 5 Oct 2010; accepted 5 Oct 2010; published 12 Oct 2010

diffraction) Fourier harmonics of the object grating were measured at the wavelengths accessible by our $^{13}CO_2$ laser in the 10.7 μm < λ < 11.3 μm spectral range. All signals were corrected for the different distance from the sample to the detector and normalized to the signal from the incoming radiation with no sample. Absolute transmission coefficients for these modes are plotted in Fig. 5(a), while the same transmission coefficients normalized to that of the diffraction-limited 0th mode are plotted in Fig. 5(b). The line-tunable CO_2 laser (blue symbols) was used for measuring the absolute transmission of the diffraction-limited order (0th harmonic) as shown in Fig. 5(a), and a broadband thermal source (FTIR, solid blue line) was used to confirm the laser experiment, showing excellent agreement. Transmission through the Type 2 IPM is almost an order of magnitude smaller than through the Type 1 IPM, which is expected because diffraction-limited waves are evanescent in the former but propagating in the latter, as depicted in Fig. 1(b). On the other hand, sub-diffraction waves (1st and 2nd Fourier components of the *object* grating) are propagating in both types of IPMs. That explains why the ratio of 1st to 0th order harmonics changes from 0.02 at 10.7 μm to 0.4 at 11.31 μm, which is a factor of 20 enhancement.

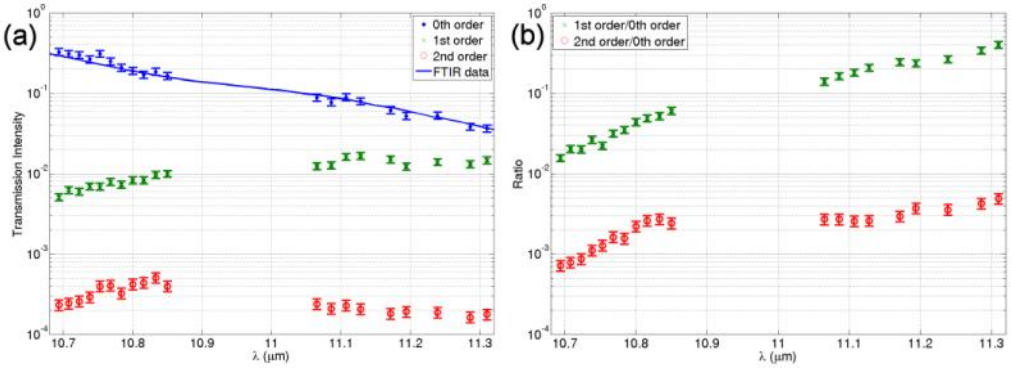

Fig. 5. Experimental demonstration of the anti-cutoff [13] phenomenon. (a) Normalized intensities of Fourier harmonics vs wavelength. (b) Ratio of 1st to 0th and 2nd to 0th Fourier harmonics vs wavelength.

Next, phase characteristics of wave transmission through the IPM were investigated. When a sub-diffraction or diffraction-limited wave propagates through the IPM, it acquires the phase φ_m given by Eq. (3). The standard approach to measuring this phase is interferometry: a reference beam interferes with a beam that interacts with the sample. The result yields φ_m if the relative phase of the incident and reference beams is known. This relative phase difference depends on the geometric path difference and can be difficult to accurately measure and control. Recently, a new method of measuring the absolute phase in heterodyne-detected transient grating experiments has been introduced [31]. We used this type of approach to measure phase shifts between 0th and 1st Fourier orders $\varphi_0 - \varphi_1$. The experimental set-up is schematically illustrated in Fig. 6: the IPM is installed inside a Mach-Zehnder interferometer which consists of two beam arms. One beam passes through a delay line which adds a variable amount of phase relative to the non-delayed beam. The sample is aligned such a way that the 0th order mode produced by the delayed beam being transmitted through the IPM is collinear and coincident with the −1st order mode of the non-delayed arm. The intensity of these interfering beams is measured by Detector 1. The electric field incident on Detector 1 is

$$E_{D1} = E_{D1}^{0} e^{i\varphi_0 + i\varphi_d - i\omega t} + E_{D1}^{-1} e^{i\varphi_{-1} - i\omega t}, \qquad (4)$$

#133245 - $15.00 USD Received 12 Aug 2010; revised 5 Oct 2010; accepted 5 Oct 2010; published 12 Oct 2010

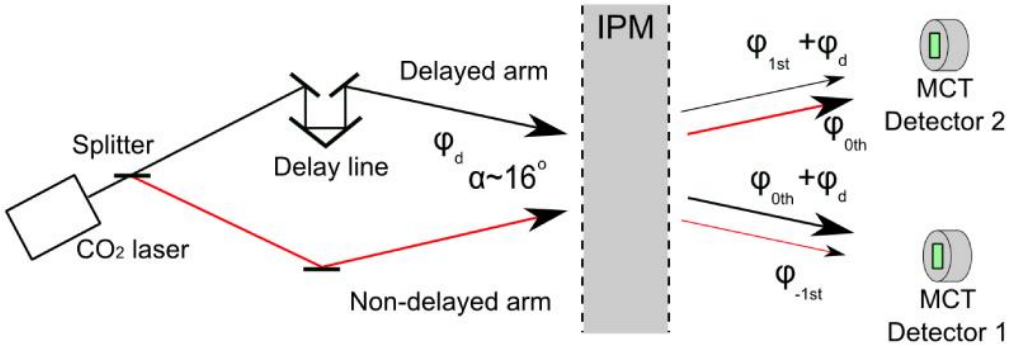

Fig. 6. Experimental set-up for phase measurements.

where the complex amplitudes of the 0th order E_{D1}^{0} and the -1^{st} order E_{D1}^{-1} have the same phase. The phase difference acquired after the beam splitter by simple path length difference (including the optical delay line) is incorporated in φ_d. The absolute value of the two amplitudes E_{D1}^{0} and E_{D1}^{-1} is different in general since the 0th and -1^{st} order modes have different transmission intensities through the IPM. From Eq. (4) we see that the intensity measured at Detector 1 is

$$I_{D1} = \left|E_{D1}\right|^2 = \left|E_{D1}^{0}\right|^2 + \left|E_{D1}^{-1}\right|^2 + 2\left|E_{D1}^{0}E_{D1}^{-1*}\right|\cos(\varphi_d + \varphi_0 - \varphi_{-1}), \qquad (5)$$

where φ_0 and $\varphi_{-1} = \varphi_1$ (due to grating symmetry) are, respectively, phase advances of the 0th (diffraction-limited) and -1^{st} (sub-diffraction) modes given by Eq. (3). Recalling that $\left|E_{D1}^{0}\right|^2$ and $\left|E_{D1}^{-1}\right|^2$ are in fact the intensities of the transmitted radiation of 0th order from delayed arm $I_{del,1}^{0}$ and -1^{st} order from non-delayed arm $I_{non-del,1}^{-1}$, respectively, we can re-write Eq. (5)

$$I_{D1} = I_{del,1}^{0} + I_{non-del,1}^{-1} + 2\sqrt{I_{del,1}^{0} I_{non-del,1}^{-1}}\cos(\varphi_d + \varphi_0 - \varphi_1).$$

Similarly, the beam incident upon Detector 2 is a combination of a non-delayed beam that was transmitted through the IPM (0th order) and a delayed beam that was diffracted through the IPM (1st order). The combined electric field of these two beams that reaches Detector 2 is

$$E_{D2} = E_{D2}^{0} e^{i\varphi_0 - i\omega t} + E_{D2}^{1} e^{i\varphi_1 + \varphi_d - i\omega t}.$$

The intensity measured at Detector 2 is

$$I_{D2} = \left|E_{D2}\right|^2 = \left|E_{D2}^{0}\right|^2 + \left|E_{D2}^{1}\right|^2 + 2\left|E_{D2}^{0}E_{D2}^{1*}\right|\cos(\varphi_d - \varphi_0 + \varphi_1),$$

which can be re-written as

$$I_{D2} = I_{non-del,2}^{0} + I_{del,2}^{1} + 2\sqrt{I_{non-del,2}^{0} I_{del,2}^{1}}\cos(\varphi_d - \varphi_0 + \varphi_1).$$

Again, we emphasize that φ_d includes all phase information regarding differences in path between the beam splitter and the IPM. This can be varied by changing the length of the delay line and doing so allows us to measure $\varphi_0 - \varphi_1$. The procedure to do so is as follows. We measured the intensities of the beam incident upon detectors 1 and 2 while varying the delay line length. Figure 7 shows the intensities measured by detectors 1 and 2 as a function of phase delay added by the delay line. The two intensities vary from their average value by the cosine of φ_d plus a shift. According to Eq. (5), the phase of the cosine wave measured by Detector 1 is $\phi_{D1} = \varphi_d + \varphi_0 - \varphi_1$, and shifted forward by $\varphi_0 - \varphi_1$. As for Detector 2, the phase

#133245 - $15.00 USD Received 12 Aug 2010; revised 5 Oct 2010; accepted 5 Oct 2010; published 12 Oct 2010

of the cosine is $\phi_{D2} = \varphi_d + \varphi_1 - \varphi_0$, so it is shifted backwards by $\varphi_0 - \varphi_1$. When these two intensities are plotted on the same graph, the phase shift of $\phi_{D1} - \phi_{D2} = 2(\varphi_0 - \varphi_1)$ between them can be measured, allowing us to calculate $\varphi_0 - \varphi_1$.

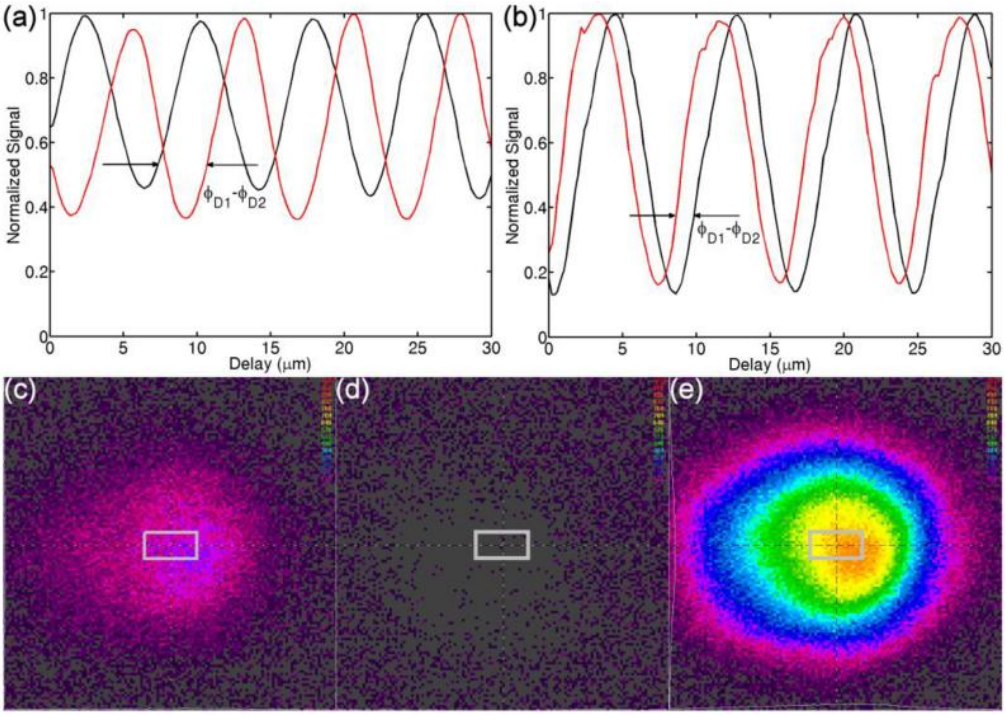

Fig. 7. Signals from Detector 1 (red) and Detector 2 (black) at (a) λ=10.753 μm and (b) λ=11.107 μm. Note the sign change of the phase shift between the detector signals $\phi_{D1} - \phi_{D2}$. Beam profile measured near Detector 1 for λ=11.171 μm: (c) single (delayed) arm only, (d) interference minimum, and (e) interference maximum. The grey rectangle in the center represents the size of the MCT detector relative to the beam.

Alignment of the two beams is crucial for accurate interference (Fig. 7(a,b)); good quality interference pattern ("infinite fringe" condition, Fig. 7(c-e)) was achieved and observed with a pyro-electric camera. Figures 7(c-e) shows the intensities of the interfering radiation near Detector 1 for the relative phase delays φ_d corresponding to the minimum (d) and in the maximum (e) of intensity at λ=11.171 μm. For comparison, the single beam intensity (delayed arm only) is presented in (c). The grey rectangle in the center represents the sensitive area of the MCT detectors compared to the beam size.

The normalized signals $I_{D1,2}$ (φ_d, λ) from Detectors 1 and 2 were plotted side by side as a function of φ_d for 15 laser wavelengths. Two such plots are shown in Fig. 7: (a) for λ=10.753 μm (corresponding to Type 1 IPM) and (b) for λ=11.107 μm (corresponding to Type 2 IPM). Note that the sign of the phase shift between the detector signals $\phi_{D1} - \phi_{D2}$ (red and black curves in Fig. 7(a,b)) changes. This is in accordance with the transition from positive index propagation of the m = 1 sub-diffraction wave for Type 1 IPM $\varphi_1 > 0$ to negative index propagation $\varphi_1 < 0$ for Type 2 IPM because for both types of IPMs $|\varphi_1| >> |\varphi_0|$.

Another distinguishing feature between intensity plots in Fig. 7(a) and 7(b) is that the modulation depth is much larger in Type 2 IPM. The contrast $K \equiv (I_{max} - I_{min}) / (I_{max} + I_{min})$ of the interference pattern observed by the detectors is

#133245 - $15.00 USD Received 12 Aug 2010; revised 5 Oct 2010; accepted 5 Oct 2010; published 12 Oct 2010

$$K_{D1} = \frac{2\sqrt{I^{0}_{del,1} I^{-1}_{non-del,1}}}{I^{0}_{del,1} + I^{-1}_{non-del,1}}, \quad \text{and} \quad K_{D2} = \frac{2\sqrt{I^{0}_{non-del,2} I^{1}_{del,2}}}{I^{0}_{non-del,2} + I^{1}_{del,2}} \tag{6}$$

for each of the detectors respectively. Equation (6) shows that $K_{D1} = K_{D2}$ when (i) incident radiation intensities in both arms of Mach-Zehnder interferometer are equal *or* (ii) the ratio of the 1st to 0th Fourier order is equal to 1. Neither of those conditions is satisfied in our experiments, so the interference patterns recorded by the detectors have different contrasts $K_{D1} \neq K_{D2}$ as can be seen in Fig. 7(a) and 7(b).

The contrast $K \rightarrow 1$ when the interfering $m = 1$ and $m = 0$ modes have almost-equal intensities, which is the case for Type 2 IPM as shown in Fig. 5(b) and Figs. 7(d,e). For Type 1 IPM they differ by almost two orders of magnitude (see Fig. 5). However, the amplitudes of even very weak sub-diffraction waves at λ=10.7 μm were sufficient to observe a low-contrast interference pattern with the accuracy high enough for reliable phase retrieval (see Fig. 7(a)).

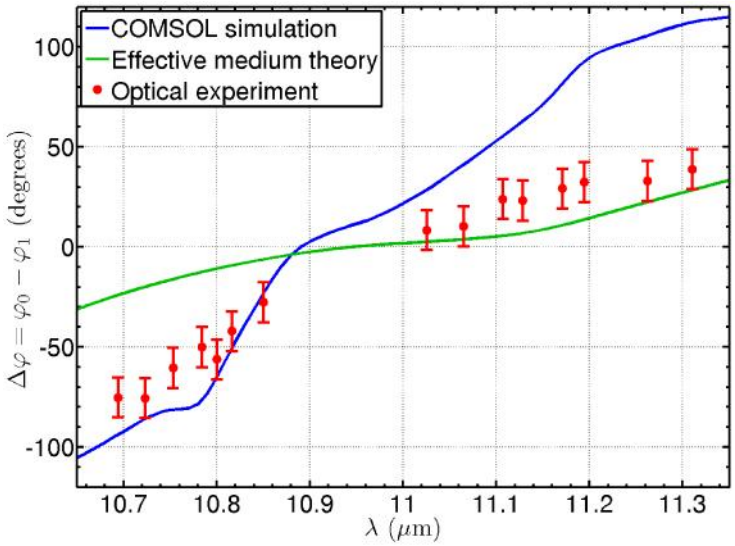

Fig. 8. Phase shift between 0th and 1st Fourier harmonics: experiment (red dots), effective medium theory (green curve) and COMSOL simulations (blue curve).

Finally, to demonstrate the transition from positive to negative refractive index as the laser is tuned from Type 1 to Type 2 IPM, we plot in Fig. 8 (red dots with error bars) the measured phase advance difference ($\varphi_0 - \varphi_1$) as a function of wavelength. The experimental data clearly indicate that the phase shift contrast changes sign around the superlensing wavelength $\lambda_s \approx 10.97$ μm, at which point the phase contrast vanishes. Although we were able to measure the phase of only one sub-diffraction wave ($m = 1$), our experimental result is in qualitative agreement with Fig. 1(b) which indicates that *all* Re $k_\perp$ curves cross at $\lambda = \lambda_s$, resulting in a zero phase contrast for all sub-diffraction waves at that wavelength. The vanishing phase contrast at λ_s for all sub-diffraction waves may explain the absence of phase contrast at superlensing that was observed in earlier [14] experiments. The experimentally observed sign change of the phase of the $m = 1$ mode shown in Fig. 8 is also consistent with the sign change of the phase contrast at the $\lambda = \lambda_s$ wavelength in superlens imaging [14] experiments.

Two additional theoretical plots are also shown in Fig. 8. The green line represents the results of the effective medium theory based on the single-pass propagation of 0th and 1st Fourier harmonics with $k_\perp^m$ calculated from Eq. (3): $\varphi_0 - \varphi_1 = \mathrm{Re}\left(k_\perp^0 - k_\perp^1\right) l$. Two main limitations of this straightforward but overly simplified theory that may cause discrepancies

#133245 - $15.00 USD Received 12 Aug 2010; revised 5 Oct 2010; accepted 5 Oct 2010; published 12 Oct 2010

are that (a) multiple reflections of the electromagnetic waves off the OG and DG are possible and (b) phase shifts may be acquired by the sub-diffraction and diffraction-limited waves upon scattering by the gratings. As evidenced by Fig. 8, the single-pass effective medium theory consistently under-estimates the experimentally observed phase shifts. The blue line represents the results of the exact numerical simulation using COMSOL finite-elements code. It accurately takes into account the above mentioned effects (a) and (b). The weakness of the numerical simulation is that it assumes that the two gratings are ideal. Unfortunately, that is not the case as can be seen from Fig. 3(d): adjacent slits are not entirely identical and, therefore, multiple reflections are likely to be suppressed. The exact COMSOL simulation consistently over-estimates the experimentally observed phase shifts. As shown in Fig. 8, the experimentally observed phase shifts fall between the two theoretical curves for all wavelengths.

6. Conclusions

In conclusion, we have fabricated an infrared Indefinite Permitivity Medium (IPM) based on the SiO_2-SiC-SiO_2 multi-layer. IPMs are promising for a variety of near-field applications that rely on sub-diffraction optical waves. Two types of uniaxial IPMs based on the layered structures have been identified: Type 1 (2) IPMs with the positive (negative) dielectric permittivity parallel to the layers. By changing the wavelength of the line-tunable CO_2 laser, both types of IPMs were experimentally accessed. We have experimentally launched sub-diffraction waves into the IPM and measured their transmission characteristics (amplitude and phase). A novel interferometric technique was used to demonstrate that sub-diffraction waves can propagate with a negative refractive index in the Type 1 IPM. We have also experimentally demonstrated the anti-cutoff phenomenon, whereby the propagating sub-diffraction waves dominate over the evanescent diffraction-limited waves in the Type 2 IPM.

Acknowledgements

The authors would like to thank Dr. Anatoli Morozov (Princeton University) for his help with the laser ablation of SiO2 mask. This work was supported by the National Science Foundation (NSF) grants CMMI-0928664 and EECS-0709323 and the U.S. Air Force Office of Scientific Research (AFOSR) MURI Grants FA9550-06-1-0279 and FA9550-08-1-0394.

#133245 - $15.00 USD Received 12 Aug 2010; revised 5 Oct 2010; accepted 5 Oct 2010; published 12 Oct 2010